

Ultrashort pulse generation from a graphene-coupled passively mode-locked terahertz laser

Elisa Riccardi,^{1*} Valentino Pistori,^{1*} Seonggil Kang,² Lukas Seitner,³ Anna De Vetter,² Christian Jirauschek,³ Juliette Mangeney,² Lianhe Li,⁴ A. Giles Davies,⁴ Edmund H. Linfield,⁴ Andrea C. Ferrari,⁵ Sukhdeep S. Dhillon,² and Miriam S. Vitiello¹

¹ NEST, CNR - Istituto Nanoscienze and Scuola Normale Superiore, Piazza San Silvestro 12, 56127, Pisa, Italy

² Laboratoire de Physique de l'Ecole Normale Supérieure, ENS, Université PSL, CNRS, Sorbonne Université, Université de Paris, Paris, France

³ Department of Electrical and Computer Engineering, Technical University of Munich, Hans-Piloly-Str. 1, 85748 Garching, Germany

⁴ School of Electronic and Electrical Engineering, University of Leeds, Leeds LS2 9JT, UK

⁵ Cambridge Graphene Centre, University of Cambridge, Cambridge CB3 0FA, UK

**These authors contributed equally to this work*

The generation of stable trains of ultra-short (fs–ps), terahertz (THz)-frequency radiation pulses, with large instantaneous intensities, is an underpinning requirement for the investigation of light-matter interactions, for metrology and for ultra-high-speed communications. In solid-state electrically-pumped lasers, the primary route for generating short pulses is through passive mode-locking. However, this has not yet been achieved in the THz range, defining one of the longest standing goals over the last two decades. In fact, the realization of passive mode-locking has long been assumed to be inherently hindered by the fast recovery times associated with the intersubband gain of THz lasers. Here, we demonstrate a self-starting miniaturized ultra-short pulse THz laser, exploiting an original device architecture that includes the surface patterning of multilayer-graphene saturable absorbers distributed along the entire cavity of a double-metal semiconductor 2.30–3.55 THz wire laser. Self-starting pulsed emission with 4.0-ps-long pulses in a compact, all-electronic, all-passive and inexpensive configuration is demonstrated.

In laser physics, mode-locking is a fundamental set of techniques that allows the generation of ultra-short light pulse trains with large instantaneous intensities from a laser source^{1–3}. Owing to their remarkable stability⁴, high peak-power^{5,6}, ultra-short duration^{7,8} and coherent emission over a broad bandwidth⁸, mode-locked laser sources benefit an exceptional variety of applications, including micro-⁹ and nano-fabrication¹⁰, optical data storage¹¹, microscopy¹²,

telecommunications¹³, surgery¹⁴ and research in ultrafast phenomena¹⁵, among many others. Most notably, frequency combs (FC)¹⁶ can be generated from stabilized mode-locked lasers¹⁷, and hence are key for quantum metrology, sensing, communication, and spectroscopy¹⁷.

Passive mode-locking techniques, relying on semiconductor saturable absorber mirrors (SESAM)¹⁸ or nonlinear phase shifts^{19–21}, are commonly used to generate ultra-short pulses from the ultraviolet (from $\lambda \sim 200\text{nm}$ ²²) to the mid-infrared (up to $\lambda \sim 3.5\mu\text{m}$ ²³). At longer wavelengths such as terahertz (THz) frequencies ($\lambda \sim 30\mu\text{m} - 300\mu\text{m}$), the lack of suitable gain media has resulted in the adoption of different strategies to generate pulsed laser radiation, either through optical rectification processes using femtosecond optical laser²⁴, although with limited ($\sim \mu\text{W}$) output power and efficiency ($\eta < 6\%$)^{25,26}, or requiring complex, non-tabletop and expensive setups, such as free electron lasers²⁷, hindering their exploitation beyond basic research.

Quantum cascade lasers (QCLs) are the only miniaturized direct sources of laser radiation in the THz frequency range, combining chip-scale size, high ($> 1\text{W}$) power emission, high spectral purity and broad bandwidth²⁸. Although room temperature operation has still to be achieved, Fabry-Perot THz QCLs can operate in a compact Peltier cooler configuration up to 250K ²⁹ and can generate trains of short pulses by active mode-locking^{30–32}, i.e. by modulating the gain and losses in the active medium with a bias current modulation. Active techniques are favored by the QCL ultrafast carrier dynamics inherent to the intersubband transitions in the gain medium³³. The gain in a QCL recovers from its saturated value much faster ($\sim 2\text{ps}$ ³⁴) than the cavity round-trip time ($\sim 72\text{ps}$ for a standard 3-mm-long cavity) and the photon lifetime³⁵. This is the result of very strong electron-electron and electron-phonon interactions in the QCL polar semiconductor gain media, which induce an ultrafast non-radiative intersubband relaxation³⁶. This, in turn, prevents the successful use of conventional passive mode-locking techniques based on lumped absorbers³⁷, since local perturbations of the photon population are quickly reabsorbed by the fast gain that quickly restores a quasi-continuous wave (CW) emission profile^{38,39}. Recent approaches for short pulse emission in THz QCLs are therefore all based on active schemes. These include dispersion compensation of the active region, leading to the generation of a train of 4-ps-long pulses³⁰, or generation of shorter isolated pulses (2.5ps)³², albeit with a duration limited by the slow electrical modulation employed in the active modelocking⁴⁰. The latter, which makes inefficient use of the gain, also requires dedicated external electronics and connections, impacting its widespread adoption.

Although self-starting short pulse emission from THz QCLs is highly desirable for spectroscopic⁴¹, imaging⁴², metrological⁴³ and Information and Communication Technologies (ICT) applications⁴⁴, and for providing a compact alternative to bulky THz time-domain systems⁴⁵, passive mode-locking in THz QCLs has not been reported to date, to the best of our knowledge. Theoretical predictions of possible design strategies (i.e. interleaved gain and absorbing periods with appropriate dipole moments)⁴⁶ have been followed by the encouraging experimental observation of Rabi-flopping in mid-IR QCLs⁴⁷. However, at THz frequencies, engineering intra-cavity semiconductor multilayers with stringent requirements of the gain and absorption faces fundamental obstacles due to the extremely small photon energies involved.

Here we demonstrate passive mode-locking in a semiconductor heterostructure laser operating at THz frequencies. By employing a heterogeneous gain medium^{48,49}, and a cavity architecture that integrates a distributed graphene saturable absorber (DGSA) on the top-surface of the double-metal QCL cavity, we achieve self-starting pulsed emission with 4.0-ps-long pulses in a compact, all-electronic, all-passive and inexpensive configuration. We take advantage of the high transparency modulation ($\sim 80\%$)⁵⁰ and ultrafast recovery time (2–3 ps)^{51–53} (i.e. faster than the gain recovery time in THz QCLs) of graphene saturable absorption, while the intracavity THz radiation experiences the saturable losses, thus favoring pulsed emission over the naturally occurring CW emission. Detailed electromagnetic simulations of the QCL structure and light-matter interactions in the active medium corroborate our findings, confirming the robustness of our approach. The proposed scheme can be applied to any semiconductor heterostructure laser, including mid-IR QCLs - with the first claims of passive mode-locking of QCLs operating in the mid-infrared⁵⁴ re-interpreted as coherent dynamic instabilities resulting from the extremely fast gain recovery time of this family of “class A” lasers^{34,35,55}.

Results

The QCL gain medium comprises 9 GaAs quantum wells, forming a cascade of alternating photon and LO-phonon-assisted transitions between two quasi-minibands^{48,56}. It consists of a 17- μm -thick GaAs/AlGaAs heterostructure with 3 active regions having gain bandwidths centered at 2.5, 3 and 3.5 THz and comparable threshold current densities. The double-metal Fabry-Perot laser cavity includes top Ni-based lossy side absorbers, to suppress high-order lateral modes (Methods)³². A reference Fabry-Perot QCL 2.9-mm-long and 85- μm -wide was fabricated with a set of 6.5- μm -wide side absorbers (see Ref.⁴⁹ for transport and optical data),

while a 2.3-mm-long and 49- μm -wide QCL with 0.5- μm -wide side absorbers was prepared for multilayer graphene (MLG) integration. Two 4- μm -wide stripes, aligned with the waveguide longitudinal axis and centered 12 μm from each edge, were lithographically defined onto the top Au layer, exposing the active region below. The DGSA was realized by transferring a seven-layer CVD-grown MLG film on top of the etched stripes (Fig. 1A,B), (Methods). MLG on the Au contact outside the stripes is removed to allow application of the bonding wires (Fig. 1A), whereas the MLG ensures a homogeneous covering of the active region (Fig. 1B).

The DGSA-QCL was simulated via COMSOL Multiphysics. The MLG is included as a transition boundary condition with refractive index \tilde{n}_g determined by THz time-domain spectroscopy (TDS) experiments (Tera K5 by MenloSystems) performed on the nominally same MLG film transferred onto an undoped GaAs substrate, resulting in $\tilde{n}_g = 16.9 + i 49.2$ at 3 THz (Supplementary Material). The highly doped n^+ layer ($n = 2 \times 10^{18}$) between the active region and the top Au contact is also included in the model. Figure 1C is the electric field intensity distribution in a cross section of the QCL cavity at 3 THz. MLG affects the electric field distribution across the interface at the active region/Au top contact/air boundary at $y = 17 \mu\text{m}$, inducing the concentration of the electric field on the MLG. Refs^{50,57} showed that a strong THz electric field can saturate the graphene absorption, α_g , which results in a decrease of the imaginary part of its complex refractive index k_g due to its proportionality to the absorption coefficient $\alpha_g = 4\pi k_g / \lambda_0$ ⁵⁸, where λ_0 is the radiation wavelength.

We then simulated the DGSA-induced waveguide losses spectra for the TM_{00} mode at 3 THz for different values of the imaginary part of the MLG refractive index (Fig. 1D). For each frequency, the losses have a maximum, marked by the black dashed line in the map. Below this curve, a reduction of $\text{Im}(\tilde{n}_g)$ corresponds to lower losses, i.e. the MLG stripes behave as a DGSA. $\text{Im}(\tilde{n}_g)$, as extracted from THz-TDS, is displayed as the purple dashed line in Fig. 1D. This guarantees DGSA operation at least for all frequencies > 2.5 THz. The TM_{00} and TM_{01} waveguide losses decrease for stronger saturation, thus leading to a net round-trip gain for pulsed over continuous wave emission. The opposite would be true if $\text{Im}(\tilde{n}_g)$ were above the loss maximum. Figure 1E shows the TM_{00} and TM_{01} mode losses at 3 THz as a function of $\text{Im}(\tilde{n}_g)$. The starting $\text{Im}(\tilde{n}_g)$ corresponds to the orange dashed line, so the $\text{TM}_{01}/\text{TM}_{00}$ ratio is 55%–60% regardless of intracavity field intensity. The saturable and non-saturable absorption coefficients can also both be extracted for the TM_{00} mode, each having an approximate value of 10.5 cm^{-1} , by comparing the losses at $\text{Im}(\tilde{n}_g) = 49.2$ and $\text{Im}(\tilde{n}_g) = 0$.

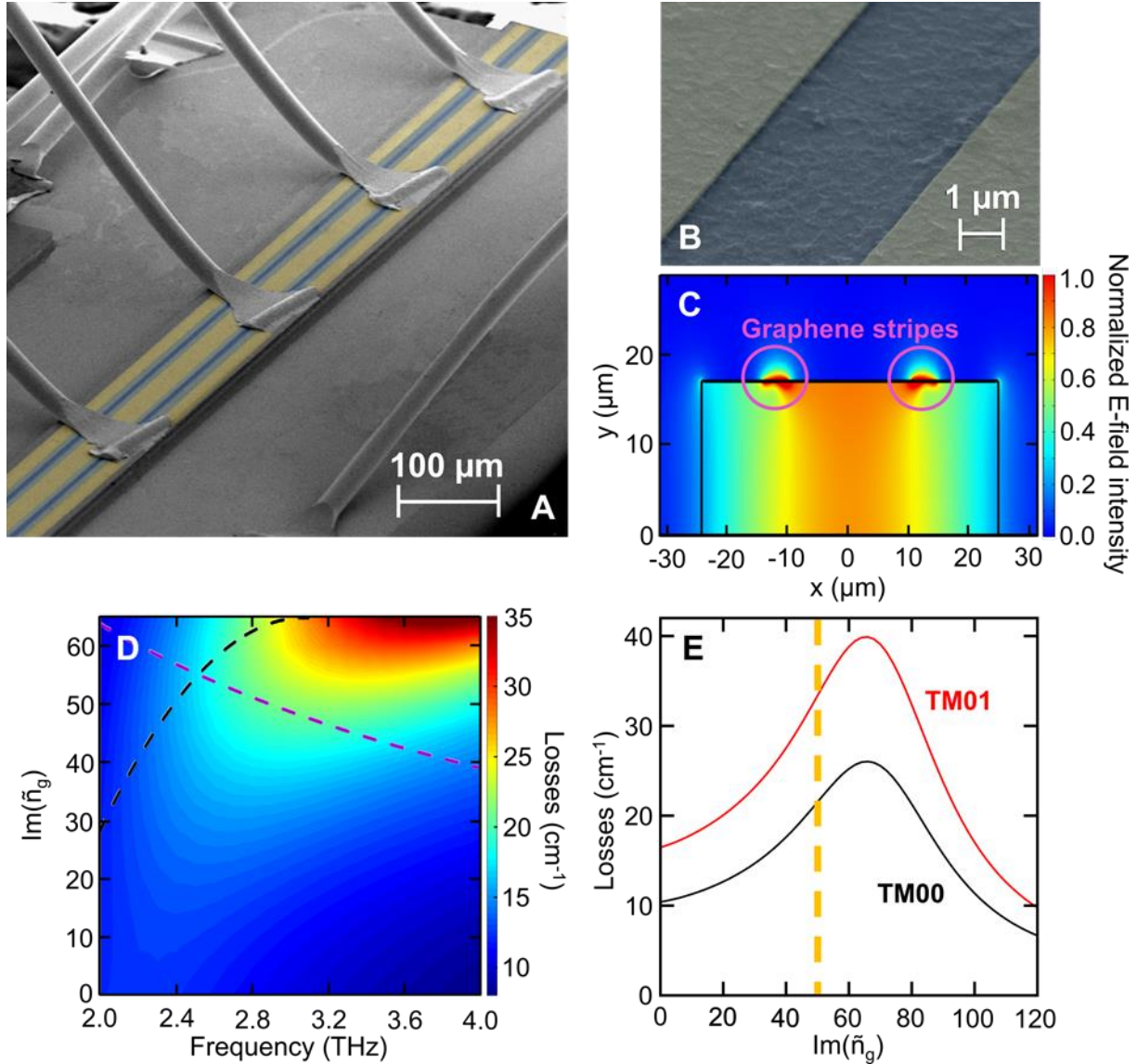


Fig. 1. Device schematic and optical simulations.

A, False color scanning electron microscope (SEM) image of a double metal QCL with an integrated DGSA. **B**, Magnified image over a portion of the QCL cavity, showing the Au top contact with the 4 μm etched stripes covered by the MLG (in blue). **C**, Simulated electric field intensity distribution in the cross-section of the DGSA-QCL at 3 THz. The violet circles highlight the MLG stripes. The MLG refractive index is set to $\tilde{n}=16.9+i49.2$ as measured via THz-TDS (see Supplementary Material). **D**, Colormap of the waveguide loss spectrum for different values of the MLG refractive index imaginary part. The black dashed line is the maximum of the losses for each frequency. The MLG operate as a DGSA when the imaginary part of the refractive index is below this line. The purple dashed line is the imaginary part of the MLG refractive index as extracted from THz-TDS experiments. **E**, Simulated waveguide losses for TM00 and TM01 modes as a function of the imaginary part for $\text{Re}(\tilde{n}_g)=16.9$ at 3 THz. For $\text{Im}(\tilde{n}_g)<65$, with $\text{Im}(\tilde{n}_g)=65$ being the loss maximum at 3 THz, a reduction of $\text{Im}(\tilde{n}_g)$, induced by saturable absorption, leads to a net round-trip gain which favours pulse formation.

Figure 2A shows the CW current density-voltage (J-V) and light-current density (L-J) characteristics of the DGSA-QCL. The threshold current density ($J_{\text{th}} \sim 170 \text{ A/cm}^2$) of the reference QCLs⁴⁹ proves that the DGSA architecture does not affect significantly J_{th} (180 A/cm^2). The QCL delivers a maximum optical power (8 mW) and has a slope efficiency of 46 mW/A.

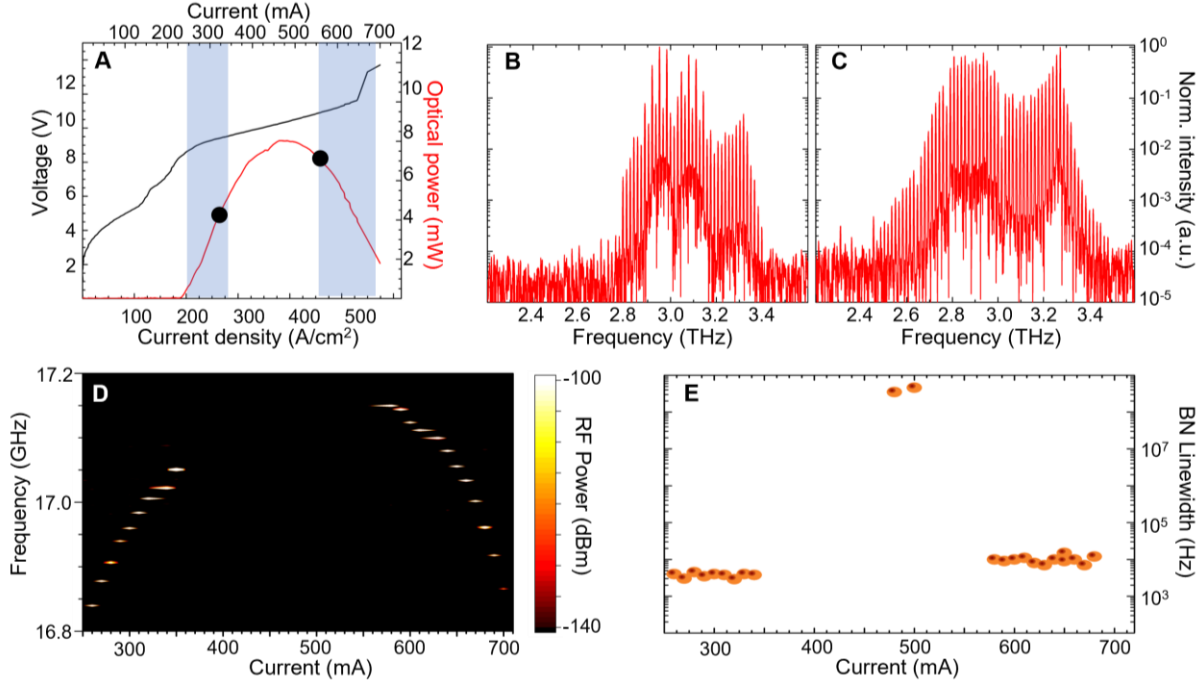


Figure 2: Electrical and optical characterization of the DGSA-QCL

A, Voltage–current density (V–J) and light–current density (L–J) characteristics measured at 20 K in continuous wave. The two shaded blue areas correspond to the bias ranges where the device shows a single and narrow intermode beatnote. The optical power was measured using a broad-area terahertz absolute power meter (TK Instruments, aperture $55 \times 40 \text{ mm}^2$). **B–C**, FTIR spectra acquired under vacuum at **(B)** 340 mA and **(C)** 570 mA at 20 K and with a 0.075 cm^{-1} spectral resolution. **D**, Intermode beatnote map as a function of the DGSA-QCL driving current, measured at 20 K. **E**, Linewidths of the beatnotes in **(D)**.

The Fourier transform infrared spectra (Bruker, Vertex 80) (Fig. 2B,C) collected under-vacuum above the whole band alignment (Fig. 2B) and in the region of maximum spectral coverage, above the peak optical power (Fig. 2C), show that the QCL bandwidth progressively increases from 0.9 to 1.25 THz. Furthermore, in these regimes, the modes appear phase-locked, as indicated by the sharp ($\sim 38 \text{ dBm}$) and narrow (1–5 kHz) intermode beatnotes (Fig. 2D,E), which provide a signature of a genuine comb operation. Generally, the emission of such a THz QCL operating as a FC is a mix of a frequency and amplitude modulated output³⁵, with a periodicity given by the cavity roundtrip.

The intermode beatnote map, plotted as a function of the driving current (Fig. 2D), shows that the comb regime in the DGSA laser persists at first for almost 100 mA, i.e. the bias region of the reference laser⁴⁹, and then immediately before and across the negative differential resistance (NDR) region. Conversely, the reference structure⁴⁹ behaves as a fully stabilized comb⁵⁹ only above the onset of band alignment and for a current range $\sim 106 \text{ mA}$ ⁴⁹, regardless of cavity dimensions^{49,60,61}. In fact, it is usually difficult to operate a QCL as a FC close to the NDR region since the high group velocity dispersion (GVD) occurring in the region of high electric field domains prevents the modes from achieving stable phase-

locking^{62,63}. In the current regime in-between (350–570 mA), the linewidth is $>10^8$ Hz, as in the reference structure for $J/J_{\text{th}} > 1.4$ ^{49,60}, signature of a mostly chaotic behavior of the modal phases.

The analysis of the beatnote linewidths shows a general agreement with the values extracted on reference lasers (2–8 kHz)^{49,60}, whereas significantly smaller linewidths (600 Hz) are obtained when GVD compensation schemes are adopted^{60,61}. This means that, as expected, the DGSA architecture does not affect the GVD and suggests that the appearance of a single and narrow beatnote at the NDR region is indicative of a different physical mechanism to that operated on the QCL by the GSA. Similar results (Supplementary Materials) have been achieved on a second DGSA-QCL with the same active region, 15 graphene layers and different cavity dimensions ($3.13 \text{ mm} \times 68 \text{ }\mu\text{m} \times 17 \text{ }\mu\text{m}$), also with significant reduction of the beatnote linewidth in the NDR.

We next measured the emission profile of the DGSA in the time domain with a coherent technique, gaining access to the amplitude and phase information of the emitted electric field. To this aim, we performed a coherent measurement based on injection seeding⁶⁴, previously used to show pulsed behavior induced in THz QCLs by active mode-locking⁶⁴. Such a technique allows measurement of the free-running QCL emission with a temporal resolution better than 100 fs.

Fig. 3A plots a 250-ps-long time-trace of the electric field emitted by the reference QCL⁴⁹ biased at 663 mA ($I/I_{\text{th}} = 1.70$), acquired 1 ns after the seeding pulse injection, i.e. well into the steady-state regime where no effect of the initial pulse persists. The quasi-CW profile combined with amplitude modulations on a short time scale (<5 ps) is a typical consequence^{65,66} of the interplay between the QCL fast gain recovery time³⁶ and the giant Kerr non-linearity⁶⁷ arising from Bloch gain⁶⁶. The spectrum (Fig. 3B), obtained by Fourier-transforming the electric field time trace, shows broadband emission from 2.2 to 3.3 THz, in agreement with the FTIR spectra measured under-vacuum^{49,60}. The latter, however, shows modes up to 3.45 THz⁶¹ and an even power distribution between the two bands centered at 2.8 and 3.2 THz, meaning that the higher frequency band is more attenuated in the TDS spectrum than the band at lower frequencies. This is consistent with the presence of the absorption at 3.7 THz of the ZnTe crystal⁶⁸ used for coherent electro-optic sampling.

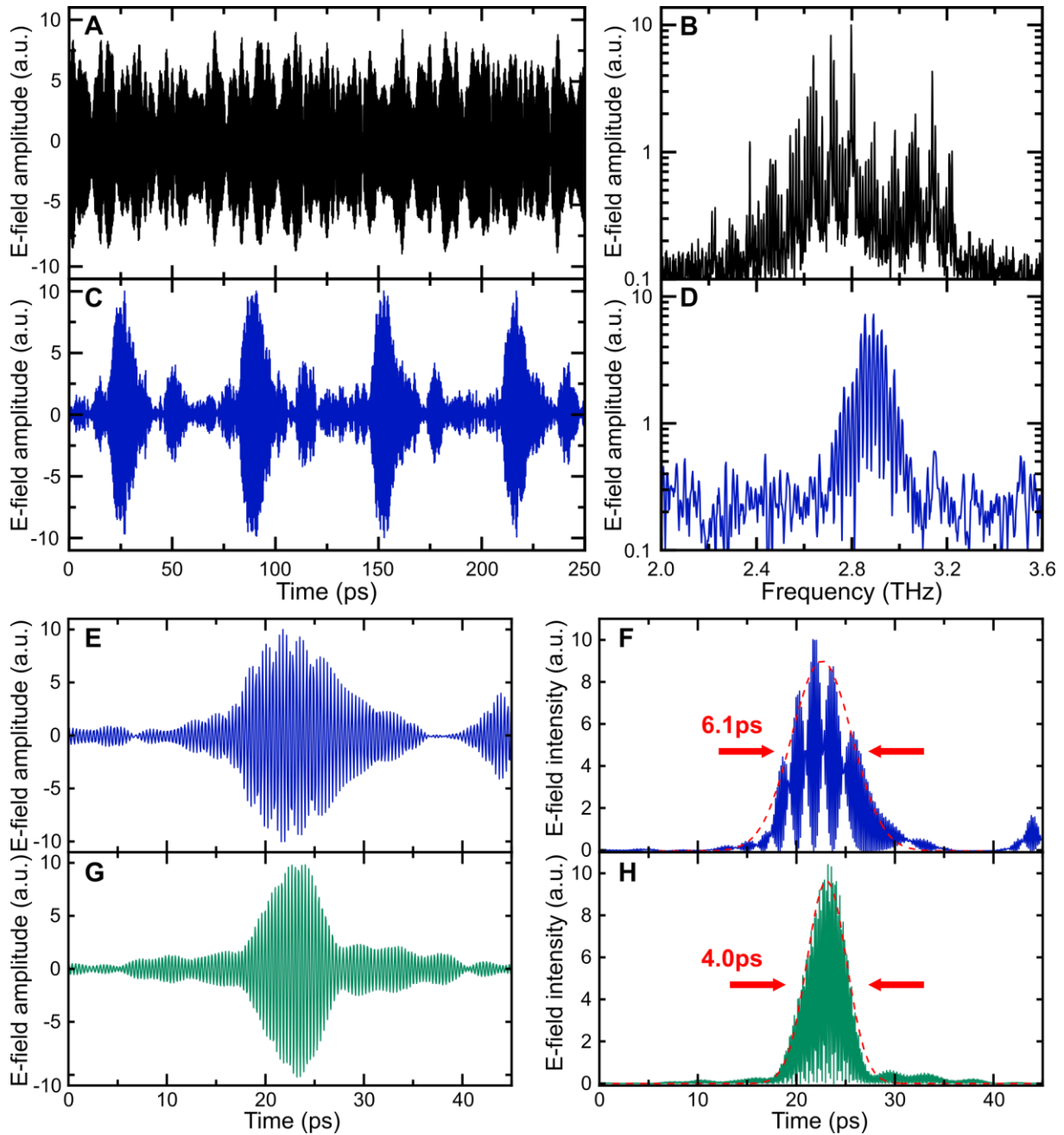


Figure 3: THz-TDS emission profiles.

A, Time-domain emission profile of the reference QCL (without GSA, Ref.⁴⁹) biased at 663 mA. **B**, Fourier frequency transform (FFT) spectrum of the time trace in Fig. 3A. **C**, Time-domain emission profile of the DGSA-QCL biased at 327 mA. **D**, FFT spectrum of the time trace in Fig. 3C. **E**, Electric field amplitude profile of a pulse emitted by the DGSA-QCL at 327 mA. **F**, Intensity profile of the pulse in Fig. 3E. The red dashed line is a Gaussian fit of the pulse with full width at half maximum (FWHM) of 6.1 ps. **G**, Electric field amplitude profile of a pulse emitted by the DGSA-QCL at 570 mA. **H**, Intensity profile of the pulse in Fig. 3G. The red dashed line is a Gaussian fit of the pulse with FWHM of 4.0 ps.

Fig. 3C plots the free-running emission of the DGSA-QCL, biased at 327 mA ($I/I_{th}=1.68$) in the regime characterized by a 3 kHz-broad beatnote. The electric field profile reveals the generation of a pulsed profile, demonstrating that the QCL can be passively mode-locked by our GSA. The spectrum retrieved by fast-Fourier transforming the electric field (Fig. 3D) matches that measured by the FTIR at the same bias (Fig. 2B), aside for the attenuation at higher frequencies due to the ZnTe crystal absorption profile. Figure 3E is the electric field amplitude profile of one of the pulses emitted by the DGSA-QCL, biased at 327 mA, ~ 1 ns after the seeding pulse injection. The corresponding pulse intensity profile is in Fig. 3F, revealing a duration of ~ 6.1 ps as extracted from a Gaussian fit (red dashed line). When the QCL is driven at 570 mA, where the number of emitted modes becomes significantly larger (Fig. 2C), the optical power per comb tooth reaches 0.12 mW and, with a sharp and narrow beatnote still present, and a pulsed behavior is once again retrieved (Fig. 3G). As expected, the broader bandwidth gets translated into a shorter pulse duration. This is evident from the intensity profile of the electric field in Fig. 3H, showing 4 ps pulse generation.

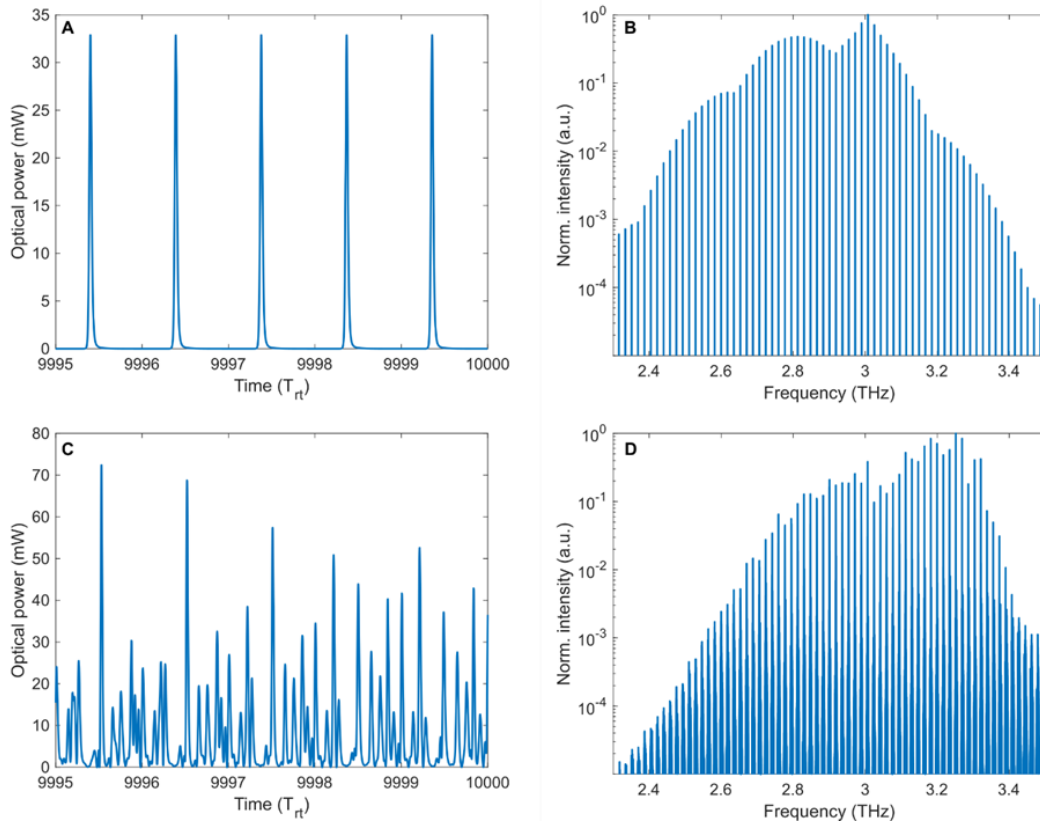


Figure 4: Maxwell-Bloch dynamical simulations.

A, Instantaneous pulse power outcoupled at the right end facet in steady state operation at ~ 2.7 times the threshold current for $P_s=85$ mW. **B**, Fourier spectrum of the time trace in Fig. 4A. **C**, Outcoupled power with increased gain showing chaotic behavior. **D**, Fourier spectrum of the time trace in Fig. 4C.

To shed light on the physical mechanism at the origin of the observed phenomenon, we performed time-domain simulations⁶⁹ to study the pulse formation mechanism of our DGSA-QCL. The active region dynamics are modeled employing a Lindblad-type approach and the quantum system represents a QCL period with periodic boundary conditions^{69,70} (Methods). The waveguide parameters used for the simulations are in Table 1. The simulated optical power of the last five roundtrip times (T_{rt}), out-coupled at the back facet in stationary operation and its Fourier transform are in Fig. 4A,B. A regular train of pulses with a duration (FWHM) ~ 1.7 ps is observed, consistent with the experimental results (4 ps).

The resulting comb shows clear, narrow (hundred Hz) and equidistant lines where 26 of them are in a 10dB power range. For comparison, enhancing the gain by increasing the doping density by $\sim 4\%$, reproduces the experimental breakdown of pulses at currents $350 \text{ mA} < I < 570 \text{ mA}$, i.e. in the current range above the breakdown of the initial comb state and before entering in the second stable comb regime, Fig. 4C,D, with the resulting chaotic behavior.

Table 1. Simulation parameters.

Waveguide parameters for our simulations.

Parameter	Value
Loss coefficient a_0	10.5 cm^{-1}
Saturable loss coefficient a_1	10.5 cm^{-1}
Saturation power P_s	85 mW
Overlap factor	0.97
Center frequency	3.2 THz
Mirror reflectivity (power)	70.88 %
Refractive index	3.6
GVD factor β_2	$1.0 \times 10^{-22} \text{ s}^2 \text{ m}^{-1}$

In order to prove quantitatively the presence of mode-locking in the simulated optical field, we employ power and phase noise quantifiers M_{σ_P} and $M_{\Delta\Phi}$,⁷¹ as:

$$M_{\sigma_P} = \frac{1}{N_{10}} \sum_{q=1}^{N_{10}} \sigma_{P_q} \quad M_{\Delta\Phi} = \frac{1}{N_{10}} \sum_{q=1}^{N_{10}} \sigma_{\Delta\Phi_q}$$

with

$$\sigma_{P_q} = \sqrt{\langle (P_q(t) - \langle P_q(t) \rangle)^2 \rangle} \quad \sigma_{\Delta\Phi_q} = \sqrt{\langle (\Delta\Phi_q(t) - \langle \Delta\Phi_q(t) \rangle)^2 \rangle}$$

where $P_q(t)$ are the modal amplitudes and $\Delta\Phi_q(t)$ the modal phase differences between one mode and the adjacent, at time t for each mode $q = 1, \dots, N_{10}$, with N_{10} being the number of modes in the -10dB spectral bandwidth.

In this framework, an optical FC is present for $M_{\sigma P} < 10^{-2}$ mW and $M_{\Delta\Phi} < 2 \times 10^{-2}$ rad. Regarding the pulsed mode of Fig. 4A,B, values of 2×10^{-8} mW and 2×10^{-6} rad are obtained. We can thus confirm an ultra-stable mode-locked operation in this current range. Calculating the same parameters for the results of Fig. 4C,D, yields $M_{\sigma P} = 0.21$ mW and $M_{\Delta\Phi} = 9.34$ rad. This increase proves the absence of mode-locking for higher gain, in agreement with our theory of pulse formation, as discussed below.

Discussion

One key observation to understand pulse formation in our DGSA-QCL is that the graphene stripes provide quasi-instantaneous saturable absorption across the resonator length, while also the gain has a recovery time much faster (a few ps) than the roundtrip time³⁴. Ref.⁷² suggests that mode-locked operation only occurs if the pulses are stabilized by a net gain window, while the standard passive mode locking theory⁷² does not provide self-starting mode-locked pulse solutions for instantaneous gain and saturable absorption. These assumptions are relaxed in our experiments by the fact that the gain, despite its fast recovery, is still slower than the saturable absorption provided by graphene^{73,74}. Thus, a narrow gain region can exist slightly above the threshold gain where self-starting mode-locked pulse operation occurs. As also pointed out in⁷², the constraints for self-starting passive mode-locking are further relaxed if a second, longer gain recovery time is present, as is typically the case for bound-to-continuum QCLs due to the electron transport across the miniband⁷⁵. Deviations from the analytical theory of Ref.⁷² arise for QCLs. In particular, the gain saturation and GSA bleaching due to the propagating pulse open up a short net gain window stabilizing the pulse, but introduce a net loss for counterpropagating fields, which helps suppress the buildup of a CW background. Furthermore, quantum coherence and nonlinear effects, spatial hole burning, as well as considerable outcoupling at the end facets, have to be taken into account necessitating our detailed Maxwell-Bloch-type simulations presented in Methods.

Aside from the experimental non-idealities, the main difference between simulated and experimental pulses can be ascribed to the available number of spectral modes and their power distribution, which is considerably more uniform in the simulations. This suggests that the main limitation in terms of achievable pulse duration is the laser bandwidth. Further

optimization of the waveguide structure, adjustments to the graphene optical properties and the employment of ultra-broadband (an octave) active regions could be adopted to enhance the emission bandwidth uniformity, effectively indicating a practical path to achieve sub-ps THz pulse generation.

Conclusions

We have shown ultrashort pulse generation from a passively modelocked semiconductor THz laser using a unique graphene based distributed saturable absorber. Exploiting the wide spectral gain of THz QCLs and the lithographic capability to embed miniaturized, highly nonlinear, intra-cavity graphene absorbers to modulate light and produce short pulses without any external source or seeding system, could allow QCLs to become an attractive alternative to present-day THz TDS systems in spectroscopic and imaging applications. This will advance quantum science enabling users to capture the ultrafast dynamics in novel material systems, even down to the nanoscale⁷⁶, or performing real-time pulsed imaging and time of flight tomography⁷⁷, or time-resolved spectroscopy of gases, complex molecules and cold samples⁷⁸. Other opportunities include the coherent control of quantum systems⁷⁹, quantum sensing and metrology where laser excitation can match the energy level splitting of molecules (and its pulsed nature can down-convert the spectrum to the RF domain⁸⁰), or for ultra high-speed THz communications^{44,81}, greatly expanding the technological impact of QCLs.

Methods

Fabrication and graphene preparation

Fabry-Perot laser bars are fabricated in a metal-metal waveguide configuration via Au-Au thermo-compression wafer bonding of a 17- μm -thick active region onto a highly doped GaAs substrate. This is followed by the removal, through a combination of mechanical lapping and wet etching, of the host GaAs substrate of a molecular-beam-epitaxially-grown (MBE) material. An $\text{Al}_{0.5}\text{Ga}_{0.5}\text{As}$ etch stop layer is then removed using HF etching. Vertical sidewalls are defined by inductively coupled plasma etching of the laser bars to provide uniform current injection. A Cr/Au (10 nm/150 nm) top contact is then deposited along the center of the ridge surface, leaving a thin region uncovered along the ridge edges and two stripes uncovered 12 μm from the center of the cavity. 3- μm -wide Ni (5-nm-thick) side absorbers were then deposited over the lateral uncovered region using a combination of optical lithography and thermal evaporation. These lossy side absorbers are intended to inhibit lasing of the higher order lateral modes by increasing their threshold gain⁸².

The multilayer graphene sample is prepared and transferred on the stripes, using a wet transfer technique: A4-950K poly(methyl-methacrylate) polymer (PMMA) is spin coated at 2000 rpm on the surface of a single layer (SLG) sample (1cm \times 1cm) grown on Cu via CVD. After 1 minute on a hot plate at 90°C, the sample is placed in a solution of 1 g of ammonium persulfate and 40 ml of DI water to etch the Cu substrate. Once the Cu etching is complete, the PMMA-SLG film is transferred in a beaker with DI water and then lifted with a second Cu-graphene square to obtain a bilayer graphene sample. This sample is left to dry overnight and finally the PMMA is removed with acetone. The Cu of the bilayer graphene is etched with the same technique, and then lifted by another SLG on Cu. This

process is repeated until the desired MLG thickness is reached, in our case seven layers. The MLG is transferred onto the QCL top contact and then removed from the sides of the laser cavity and from the top Au contact by oxygen reactive ion etching (RIE).

The backside of the substrate is then lapped down to 150 μm for thermal management and enable operation in CW. Laser bars, 50 μm wide and 2.2 mm long, are then cleaved and the device mounted on a copper bar, wire bonded, and then mounted onto the cold finger of a He continuous-flow cryostat.

Model

The active region dynamics is modeled based on a Lindblad-type approach, where the quantum system represents a QCL period with periodic boundary conditions^{69,70}. We performed self-consistent carrier transport simulations of the active region to extract the corresponding eigenenergies, optical dipole moments as well as the scattering and dephasing rates⁶⁹. For simplicity, the dynamical model only takes into account the 2.5 THz design, yielding agreement with experiments. The model system comprises 9 quantized energy states, including two upper- and one lower-laser levels. In the common rotating wave/slowly varying amplitude approximation, the optical cavity field is described by complex amplitudes $E^\pm(z,t)$ for the forward and backward traveling electric field component, and the propagation given by⁷⁰:

$$v_g^{-1} \partial_t E^\pm \pm \partial_z E^\pm = p^\pm - a(P)E^\pm - i \frac{\beta_2}{2} \partial_t^2 E^\pm \quad (1)$$

Here, z and t are the propagation coordinate and time, v_g denotes the group velocity, $p^\pm(z,t)$ is computed from the Lindblad equation^{69,70} and contains the polarization due to the quantized states of the QCL active region, and β_2 describes the background group velocity dispersion. The quasi-instantaneous SA is modeled by the power loss coefficient⁸³:

$$a(P) = a_0 + \frac{a_1}{1+P/P_s} \quad (2)$$

with the optical power $P \propto |E^+|^2 + |E^-|^2$. Electromagnetic simulations yield $a_0 = a_1 = 10.5 \text{cm}^{-1}$ (Fig. 1E). The saturation power P_s depends on the electric field strength and orientation in the graphene stripes, hence it does not correspond to the saturation intensity of the MLG itself as it could be retrieved through z-scan measurements or from considerations on the number of layers and doping level, but rather to the effective value for the transverse waveguide mode. Thus, we use P_s as the only fitting parameter in our simulation. The resulting Maxwell-Bloch-type model is numerically solved over ten thousand roundtrips to ensure convergence to steady state⁶⁹.

Acknowledgements This work was supported by the European Research Council through the ERC Consolidator Grant (681379) SPRINT (MSV), FET Open project EXTREME IR (944735) (MSV, SSD), ERC GSYNCOR (ACF), HETERO2D (ACF), EIC CHARM (ACF), the French National Research Agency (ANR-18-CE24-0013-02 - ‘‘TERASEL’’ (SD), and the EPSRC (UK) programme grant ‘HyperTerahertz’ (EP/P021859/1) (EHL, LL, AGD), EP/L016087/1, EP/K01711X/1, EP/K017144/1, EP/N010345/1, EP/V000055/1 (ACF), and Graphene Flagship (MSV, ACF)

Author contributions:

M.S.V. and V.P. conceived the concept. E.R. fabricated the devices, set up the transport and optical experiment. V.P. performed numerical simulations and interpreted the data. E.R. S.S.D., S.K. A.D.V.

acquired the experimental data. L.L, A.G.D. and E.H.L grew by molecular beam epitaxy the QCL structure. C.J. and L. L. developed the theoretical model. The manuscript was written by M.S.V. and V.P. M.S.V. coordinated and supervised the project. All authors contributed to the final version of the manuscript and to discuss the results.

Supporting Information Available

The following files are available free of charge. SupportingInfo.pdf

Competing financial interests:

The authors declare no competing financial interests.

Data and materials availability The data presented in this study are available on reasonable request from the corresponding author.

References and Notes

1. Lamb, W. E. Theory of an Optical Maser. *Phys. Rev.* **134**, A1429–A1450 (1964).
2. Haus, H. A. Mode-locking of lasers. *IEEE J. Sel. Top. Quantum Electron.* **6**, 1173–1185 (2000).
3. Perego, A. M. *et al.* Coherent master equation for laser modelocking. *Nat. Commun.* **11**, 311 (2020).
4. Cundiff, S. T. & Ye, J. Phase stabilization of mode-locked lasers. *J. Mod. Opt.* **52**, 201–219 (2005).
5. Du, T. *et al.* 1.2-W average-power, 700-W peak-power, 100-ps dissipative soliton resonance in a compact Er:Yb co-doped double-clad fiber laser. *Opt. Lett.* **42**, 462–465 (2017).
6. Tang, W. *et al.* High-peak-power mode-locking pulse generation in a dual-loss-modulated laser with BP-SA and EOM. *Opt. Lett.* **42**, 4820–4823 (2017).
7. Morgner, U. *et al.* Sub-two-cycle pulses from a Kerr-lens mode-locked Ti:sapphire laser. *Opt. Lett.* **24**, 411–413 (1999).
8. Rausch, S. *et al.* Controlled waveforms on the single-cycle scale from a femtosecond oscillator. *Opt. Express* **16**, 9739–9745 (2008).
9. Raciukaitis, G. Ultra-Short Pulse Lasers for Microfabrication: A Review. *IEEE J. Sel. Top. Quantum Electron.* **PP**, 1–1 (2021).
10. Gan, Z., Cao, Y., Evans, R. A. & Gu, M. Three-dimensional deep sub-diffraction optical beam lithography with 9 nm feature size. *Nat. Commun.* **4**, 2061 (2013).

11. Strickler, J. H. & Webb, W. W. Three-dimensional optical data storage in refractive media by two-photon point excitation. *Opt. Lett.* **16**, 1780–1782 (1991).
12. Otomo, K. *et al.* High-peak-power 918-nm laser light source based two-photon spinning-disk microscopy for green fluorophores. *Biochem. Biophys. Res. Commun.* **529**, 238–242 (2020).
13. Mollenauer, L. F. *et al.* Demonstration of massive wavelength-division multiplexing over transoceanic distances by use of dispersion-managed solitons. *Opt. Lett.* **25**, 704–706 (2000).
14. Uchugonova, A. *et al.* Nanosurgery of cells and chromosomes using near-infrared twelve-femtosecond laser pulses. *J. Biomed. Opt.* **17**, 101502 (2012).
15. Zewail, A. H. Femtochemistry: Atomic-Scale Dynamics of the Chemical Bond. *J. Phys. Chem. A* **104**, 5660–5694 (2000).
16. Hänsch, T. W. Nobel Lecture: Passion for precision. *Rev. Mod. Phys.* **78**, 1297–1309 (2006).
17. Fortier, T. & Baumann, E. 20 years of developments in optical frequency comb technology and applications. *Commun. Phys.* **2**, 1–16 (2019).
18. Keller, U. *et al.* Semiconductor saturable absorber mirrors (SESAM's) for femtosecond to nanosecond pulse generation in solid-state lasers. *IEEE J. Sel. Top. Quantum Electron.* **2**, 435–453 (1996).
19. Komarov, A., Leblond, H. & Sanchez, F. Passive harmonic mode-locking in a fiber laser with nonlinear polarization rotation. *Opt. Commun.* **267**, 162–169 (2006).
20. Haus, H. A., Fujimoto, J. G. & Ippen, E. P. Structures for additive pulse mode locking. *JOSA B* **8**, 2068–2076 (1991).
21. Spence, D. E., Kean, P. N. & Sibbett, W. 60-fsec pulse generation from a self-mode-locked Ti:sapphire laser. *Opt. Lett.* **16**, 42–44 (1991).
22. Lu, H., Xu, H., Zhao, J. & Hou, D. A Deep Ultraviolet Mode-locked Laser Based on a Neural Network. *Sci. Rep.* **10**, 116 (2020).
23. Qin, Z. *et al.* Black phosphorus Q-switched and mode-locked mid-infrared Er:ZBLAN fiber laser at 3.5 μm wavelength. *Opt. Express* **26**, 8224–8231 (2018).
24. Fülöp, J. A., Tzortzakis, S. & Kampfrath, T. Laser-Driven Strong-Field Terahertz Sources. *Adv. Opt. Mater.* **8**, 1900681 (2020).

25. Huang, S.-W. *et al.* High conversion efficiency, high energy terahertz pulses by optical rectification in cryogenically cooled lithium niobate. *Opt. Lett.* **38**, 796–798 (2013).
26. Gollner, C. *et al.* Highly efficient THz generation by optical rectification of mid-IR pulses in DAST. *APL Photonics* **6**, 046105 (2021).
27. Vinokurov, N. Free Electron Lasers as a High-power Terahertz Sources. *J. Infrared Millim. Terahertz Waves* **32**, 1123–1143 (2011).
28. Vitiello, M. S. & Tredicucci, A. Physics and technology of Terahertz quantum cascade lasers. *Adv. Phys. X* **6**, 1893809 (2021).
29. Khalatpour, A., Paulsen, A. K., Deimert, C., Wasilewski, Z. R. & Hu, Q. High-power portable terahertz laser systems. *Nat. Photonics* **15**, 16–20 (2021).
30. Wang, F. *et al.* Short Terahertz Pulse Generation from a Dispersion Compensated Modelocked Semiconductor Laser. *Laser Photonics Rev.* **11**, 1700013 (2017).
31. Barbieri, S. *et al.* Coherent sampling of active mode-locked terahertz quantum cascade lasers and frequency synthesis. *Nat. Photonics* **5**, 377–377 (2011).
32. Bachmann, D. *et al.* Short pulse generation and mode control of broadband terahertz quantum cascade lasers. *Optica* **3**, 1087 (2016).
33. Wang, F. *et al.* Ultrafast response of harmonic modelocked THz lasers. *Light Sci. Appl.* **9**, 51 (2020).
34. Riepl, J. *et al.* Field-resolved high-order sub-cycle nonlinearities in a terahertz semiconductor laser. *Light Sci. Appl.* **10**, 246 (2021).
35. Piccardo, M. & Capasso, F. Laser Frequency Combs with Fast Gain Recovery: Physics and Applications. *Laser Photonics Rev.* **16**, 2100403 (2022).
36. Derntl, C. G. *et al.* Gain dynamics in a heterogeneous terahertz quantum cascade laser. *Appl. Phys. Lett.* **113**, 181102 (2018).
37. Tzenov, P. *et al.* Passive and hybrid mode locking in multi-section terahertz quantum cascade lasers. *New J. Phys.* **20**, 053055 (2018).

38. Henry, N., Burghoff, D., Hu, Q. & Khurgin, J. B. Study of Spatio-Temporal Character of Frequency Combs Generated by Quantum Cascade Lasers. *IEEE J. Sel. Top. Quantum Electron.* **25**, 1–9 (2019).
39. Wang, C. Y. *et al.* Mode-locked pulses from mid-infrared Quantum Cascade Lasers. *Opt. Express* **17**, 12929–12943 (2009).
40. Kuizenga, D. & Siegman, A. FM and AM mode locking of the homogeneous laser - Part I: Theory. *IEEE J. Quantum Electron.* **6**, 694–708 (1970).
41. Theuer, M., Harsha, S. S., Molter, D., Torosyan, G. & Beigang, R. Terahertz Time-Domain Spectroscopy of Gases, Liquids, and Solids. *ChemPhysChem* **12**, 2695–2705 (2011).
42. Guerboukha, H., Nallappan, K. & Skorobogatiy, M. Toward real-time terahertz imaging. *Adv. Opt. Photonics* **10**, 843–938 (2018).
43. Consolino, L., Bartalini, S. & De Natale, P. Terahertz Frequency Metrology for Spectroscopic Applications: a Review. *J. Infrared Millim. Terahertz Waves* **38**, 1289–1315 (2017).
44. Seeds, A. J., Shams, H., Fice, M. J. & Renaud, C. C. TeraHertz Photonics for Wireless Communications. *J. Light. Technol.* **33**, 579–587 (2015).
45. Neu, J. & Schmuttenmaer, C. A. Tutorial: An introduction to terahertz time domain spectroscopy (THz-TDS). *J. Appl. Phys.* **124**, 231101 (2018).
46. Talukder, M. A. & Menyuk, C. R. Self-induced transparency modelocking of quantum cascade lasers in the presence of saturable nonlinearity and group velocity dispersion. *Opt. Express* **18**, 5639 (2010).
47. Choi, H. *et al.* Ultrafast Rabi flopping and coherent pulse propagation in a quantum cascade laser. *Nat. Photonics* **4**, 706–710 (2010).
48. Li, L. *et al.* Broadband heterogeneous terahertz frequency quantum cascade laser. *Electron. Lett.* **54**, (2018).
49. Garrasi, K. *et al.* High Dynamic Range, Heterogeneous, Terahertz Quantum Cascade Lasers Featuring Thermally Tunable Frequency Comb Operation over a Broad Current Range. *ACS Photonics* **6**, 73–78 (2019).

50. Bianchi, V. *et al.* Terahertz saturable absorbers from liquid phase exfoliation of graphite. *Nat. Commun.* **8**, 15763 (2017).
51. Hwang, H. Y. *et al.* Nonlinear THz Conductivity Dynamics in P-Type CVD-Grown Graphene. *J. Phys. Chem. B* **117**, 15819–15824 (2013).
52. Brida, D. *et al.* Ultrafast collinear scattering and carrier multiplication in graphene. *Nat. Commun.* **4**, 1987 (2013).
53. Tomadin, A., Brida, D., Cerullo, G., Ferrari, A. C. & Polini, M. Nonequilibrium dynamics of photoexcited electrons in graphene: Collinear scattering, Auger processes, and the impact of screening. *Phys. Rev. B* **88**, 035430 (2013).
54. Paiella Roberto *et al.* Self-Mode-Locking of Quantum Cascade Lasers with Giant Ultrafast Optical Nonlinearities. *Science* **290**, 1739–1742 (2000).
55. Wang, C. Y. *et al.* Coherent instabilities in a semiconductor laser with fast gain recovery. *Phys. Rev. A* **75**, 031802 (2007).
56. Wienold, M. *et al.* Low-voltage terahertz quantum-cascade lasers based on LO-phonon-assisted interminiband transitions. *Electron. Lett.* **45**, 1030–1031 (2009).
57. Hafez, H. A. *et al.* Terahertz Nonlinear Optics of Graphene: From Saturable Absorption to High-Harmonics Generation. *Adv. Opt. Mater.* **8**, 1900771 (2020).
58. Hecht, E. *Optics*. (Addison-Wesley, 2002).
59. Consolino, L. *et al.* Fully phase-stabilized quantum cascade laser frequency comb. *Nat. Commun.* **10**, 1–7 (2019).
60. Mezzapesa, F. P. *et al.* Terahertz Frequency Combs Exploiting an On-Chip, Solution-Processed, Graphene-Quantum Cascade Laser Coupled-Cavity. *ACS Photonics* **7**, 3489–3498 (2020).
61. Di Gaspare, A. *et al.* Tunable, Grating-Gated, Graphene-On-Polyimide Terahertz Modulators. *Adv. Funct. Mater.* **31**, 2008039 (2021).
62. Burghoff, D., Yang, Y., Reno, J. L. & Hu, Q. Dispersion dynamics of quantum cascade lasers. *Optica* **3**, 1362 (2016).
63. Bachmann, D. *et al.* Dispersion in a broadband terahertz quantum cascade laser. *Appl. Phys. Lett.* **109**, 221107 (2016).

64. Oustinov, D. *et al.* Phase seeding of a terahertz quantum cascade laser. *Nat. Commun.* **1**, 69 (2010).
65. Beiser, M., Opačak, N., Hillbrand, J., Strasser, G. & Schwarz, B. Engineering the spectral bandwidth of quantum cascade laser frequency combs. *Opt. Lett.* **46**, 3416–3419 (2021).
66. Opačak, N., Cin, S. D., Hillbrand, J. & Schwarz, B. Frequency Comb Generation by Bloch Gain Induced Giant Kerr Nonlinearity. *Phys. Rev. Lett.* **127**, 093902 (2021).
67. Cavalié, P. *et al.* High order sideband generation in terahertz quantum cascade lasers. *Appl. Phys. Lett.* **102**, 221101 (2013).
68. Gallot, G., Zhang, J., McGowan, R. W., Jeon, T.-I. & Grischkowsky, D. Measurements of the THz absorption and dispersion of ZnTe and their relevance to the electro-optic detection of THz radiation. *Appl. Phys. Lett.* **74**, 3450–3452 (1999).
69. Tzenov, P., Burghoff, D., Hu, Q. & Jirauschek, C. Time domain modeling of terahertz quantum cascade lasers for frequency comb generation. *Opt. Express* **24**, 23232–23247 (2016).
70. Jirauschek, C., Riesch, M. & Tzenov, P. Optoelectronic Device Simulations Based on Macroscopic Maxwell–Bloch Equations. *Adv. Theory Simul.* **2**, 1900018 (2019).
71. Silvestri, C., Columbo, L. L., Brambilla, M. & Gioannini, M. Coherent multi-mode dynamics in a quantum cascade laser: amplitude- and frequency-modulated optical frequency combs. *Opt. Express* **28**, 23846–23861 (2020).
72. Haus, H. A. Theory of mode locking with a fast saturable absorber. *J. Appl. Phys.* **46**, 3049–3058 (1975).
73. Pogna, E. A. A. *et al.* Hot-Carrier Cooling in High-Quality Graphene Is Intrinsically Limited by Optical Phonons. *ACS Nano* **15**, 11285–11295 (2021).
74. Sun, Z. *et al.* Graphene Mode-Locked Ultrafast Laser. *ACS Nano* **4**, 803–810 (2010).
75. Choi, H. *et al.* Gain Recovery Dynamics and Photon-Driven Transport in Quantum Cascade Lasers. *Phys. Rev. Lett.* **100**, 167401 (2008).
76. Pogna, E. A. A. *et al.* Mapping propagation of collective modes in Bi₂Se₃ and Bi₂Te_{2.2}Se_{0.8} topological insulators by near-field terahertz nanoscopy. *Nat. Commun.* **12**, 6672 (2021).

77. Takayanagi, J. *et al.* High-resolution time-of-flight terahertz tomography using a femtosecond fiber laser. *Opt. Express* **17**, 7533–7539 (2009).
78. Woerner, M., Kuehn, W., Bowlan, P., Reimann, K. & Elsaesser, T. Ultrafast two-dimensional terahertz spectroscopy of elementary excitations in solids. *New J. Phys.* **15**, 025039 (2013).
79. Mootz, M., Luo, L., Wang, J. & Perakis, Ilias E. Visualization and quantum control of light-accelerated condensates by terahertz multi-dimensional coherent spectroscopy. *Commun. Phys.* **5**, 1–10 (2022).
80. Consolino, L. *et al.* Quantum cascade laser based hybrid dual comb spectrometer. *Commun. Phys.* **3**, 1–9 (2020).
81. Nagatsuma, T. *et al.* Terahertz wireless communications based on photonics technologies. *Opt. Express* **21**, 23736–23747 (2013).
82. Holzwarth, R. *et al.* Optical Frequency Synthesizer for Precision Spectroscopy. *Phys. Rev. Lett.* **85**, 2264–2267 (2000).
83. Kurtner, F. X., der Au, J. A. & Keller, U. Mode-locking with slow and fast saturable absorbers-what's the difference? *IEEE J. Sel. Top. Quantum Electron.* **4**, 159–168 (1998).